

# AN OVERVIEW OF EXISTING ALGORITHMS FOR RESOLVING THE 180° AMBIGUITY IN VECTOR MAGNETIC FIELDS: QUANTITATIVE TESTS WITH SYNTHETIC DATA

THOMAS R. METCALF<sup>1</sup>, K. D. LEKA<sup>1</sup>, GRAHAM BARNES<sup>1</sup>, BRUCE W. LITES<sup>2</sup>, MANOLIS K. GEORGIOULIS<sup>3</sup>, A. A. PEVTSOV<sup>4</sup>, G. ALLEN GARY<sup>5</sup>, JU JING<sup>6</sup>, K. S. BALASUBRAMANIAM<sup>4</sup>, JING LI<sup>7</sup>, Y. LIU<sup>8</sup>, H. N. WANG<sup>9</sup>, VALENTYNA ABRAMENKO<sup>10</sup>, VASYL YURCHYSHYN<sup>10</sup>, Y.-J. MOON<sup>11</sup>

<sup>1</sup> Northwest Research Associates, Colorado Research Associates Division, 3380 Mitchell Ln., Boulder, CO 80301 U.S.A. (metcalf@cora.nwra.com)

<sup>2</sup> High Altitude Observatory, National Center for Atmospheric Research, P.O. Box 3000, Boulder, CO 80307-3000, U.S.A.

<sup>3</sup> The Johns Hopkins University Applied Physics Laboratory, 11100 Johns Hopkins Rd., Laurel, MD 20723-6099, U.S.A.

<sup>4</sup> National Solar Observatory, Sunspot, NM 88349, U.S.A.

<sup>5</sup> NASA/MSFC/NSSTC, Marshall Space Flight Center, Huntsville, AL 35812 U.S.A.

<sup>6</sup> New Jersey Institute of Technology, Center for Solar-Terrestrial Research, 323 Martin Luther King Boulevard, Newark, NJ 07102 U.S.A.

<sup>7</sup> Institute for Astronomy, University of Hawaii, 2680 Woodlawn Dr., Honolulu, HI 96822 U.S.A.

<sup>8</sup> Stanford University, HEPL Annex, B210, Stanford, CA 94305-4085 U.S.A.

<sup>9</sup> National Astronomical Observatories, Chinese Academy of Sciences, A20 Datun Rd. Chaoyang District, Beijing 100012 China

<sup>10</sup> Big Bear Solar Observatory, New Jersey Institute of Technology, 40386 North Shore Lane, Big Bear City, CA 92314-9672 U.S.A.

<sup>11</sup> Korea Astronomy and Space Science Institute, 61-1 Hwaam-dong, Yuseong-gu, Daejeon 305-348, South Korea

Received; accepted

## Abstract.

We report here on the present state-of-the-art in algorithms used for resolving the 180° ambiguity in solar vector magnetic field measurements. With present observations and techniques, some assumption must be made about the solar magnetic field in order to resolve this ambiguity. Our focus is the application of numerous existing algorithms to test data for which the correct answer is known. In this context, we compare the algorithms quantitatively and seek to understand where each succeeds, where it fails, and why. We have considered five basic approaches: comparing the observed field to a reference field or direction, minimizing the vertical gradient of the magnetic pressure, minimizing the vertical current density, minimizing some approximation to the total current density, and minimizing some approximation to the field's divergence. Of the automated methods requiring no human intervention, those which minimize the square of the vertical current density in conjunction with an approximation for the vanishing divergence of the magnetic field show the most promise.

## Keywords:

## 1. Introduction

Observations of the vector magnetic field on the surface of the Sun are essential for understanding solar magnetic structures in general, and specifically for quantifying or even predicting solar activity. However, the component of the field perpendicular to the line-of-sight, as inferred from observations of linear polarization in magnetically sensitive spectral lines, has an inherent  $180^\circ$  ambiguity in its direction (Harvey, 1969). To fully determine the vector magnetic field, this ambiguity must be resolved. The reliable resolution of the  $180^\circ$  ambiguity is essential for upcoming space- and ground-based vector magnetic field projects such as SOLIS (Jones *et al.*, 2002), Solar-B (Ichimoto and Solar-B Team, 2005; Shimizu, 2004), SDO/HMI (Scherrer and HMI Team, 2005; <http://sdo.gsfc.nasa.gov>), and ATST (Keil *et al.*, 2003). Looking ahead to these future datasets, a workshop was held at the National Center for Atmospheric Research in Boulder, Colorado in September 2005, to assess the ability of present algorithms to accurately resolve the  $180^\circ$  ambiguity.

There is no known method for resolving the ambiguity through direct observation using the Zeeman effect, at least for the single-height observations that are the most popular and well-understood approach for inferring the solar magnetic field. Hence, to resolve the ambiguity, some further assumption on the nature of the solar magnetic field must be made. Typical assumptions focus on the spatial smoothness of the field or on minimizing the divergence of the field – the latter, for example, requires approximation when only one height of the field is measured. A number of different algorithms have been developed to resolve the ambiguity, each making various assumptions on the character of the solar magnetic field. These algorithms, and their assumptions, are detailed in Section 2.

To test their performance, the existing algorithms were applied to model vector magnetic field data and the results analyzed in a “hare and hounds” exercise. Using model data in this exercise is particularly important because the known correct answer can be compared directly to the results from each algorithm. In this paper, we briefly discuss each of the algorithms tested and the data to which the algorithms were applied. We outline quantitative metrics for judging the performance of the algorithms when the solution is known, and assess the strengths and weaknesses of each algorithm based on its scores for each of the test cases.

## 2. The Algorithms

Generally, the algorithms we consider all minimize some physical quantity in order to arrive at a resolution. In Table I, we summarize both the quantity minimized and the optimization scheme used for each method. Below, we describe in more detail how each method is implemented, noting that in some cases there are multiple

implementations of the same method. Each algorithm is given a short acronym to facilitate labeling in the tables and figures.

### 2.1. ACUTE ANGLE METHOD

Although some areas of the solar atmosphere where vector magnetic field measurements are made are clearly not force-free, let alone current-free, it is often useful to consider a potential, or linear force-free, extrapolation of the magnetic field as a reference for comparison to the observations: Acute Angle Methods resolve the  $180^\circ$  ambiguity by comparing the observed field to an extrapolated model field. The azimuth is thus resolved by requiring that some component (i.e., image-plane transverse, or heliographic-plane horizontal) of the observed field and the extrapolated field make an acute angle, i.e.,  $-90^\circ \leq \Delta\theta \leq 90^\circ$ , where  $\Delta\theta = \theta_o - \theta_e$  is the angle between the observed and extrapolated components. This condition may also be expressed as  $\mathbf{B}_t^{\text{obs}} \cdot \mathbf{B}_t^{\text{pot}} > 0$ , where  $\mathbf{B}_t^{\text{obs}}$  is the transverse or horizontal component of the observed field, and  $\mathbf{B}_t^{\text{pot}}$  is the transverse or horizontal component of the extrapolated field.

The simplest approach is to use the observed, ambiguity-free longitudinal or line-of-sight component of the magnetic field  $\mathbf{B}_l$  as a boundary condition from which to calculate the potential field. Note that the potential field generated by matching the line-of-sight field on the boundary will not be the same as the potential field generated using the normal component on the boundary unless the field truly is potential, or the magnetogram is at disk center, so the line-of-sight is the normal direction. Writing the field as the gradient of a scalar,

$$\mathbf{B} = -\nabla\Phi \quad (1)$$

guarantees that the field is potential, and substituting this into the vanishing divergence of the field

$$\nabla \cdot \mathbf{B} = 0, \quad (2)$$

gives the Laplace equation for the scalar potential:

$$\nabla^2\Phi = 0. \quad (3)$$

If the vertical component  $B_z$  of the magnetic field  $\mathbf{B}$  is specified inside an area  $S$  that lays in the plane  $(x, y)$ , one has the Neumann boundary value problem for the Laplace equation

$$\left. \frac{d\Phi}{dz} \right|_S = B_z^{\text{obs}}. \quad (4)$$

One way to solve this problem is to assume that the scalar potential decreases exponentially with height ( $\Phi \sim e^{-kz}$ ), and is periodic in the  $\hat{x}$  and  $\hat{y}$  directions. In this case, the solution can be expressed in terms of Fourier transforms of the vertical or line-of-sight field on the boundary (Alissandrakis, 1981; Gary, 1989). Clearly, the periodic boundary condition is not valid on the Sun, but the ability to directly

use the ambiguity-free line-of-sight component of the field is an advantage of this formulation. The problem of the periodic boundary condition can be alleviated by padding the observed line-of-sight field with non-vector data from an instrument with a large field-of-view (e.g. SOHO/MDI, Scherrer *et al.*, 1995), padding the boundary data with zeroes, or by assuming the walls of the extrapolation box are perfectly conducting. Each of these approximations are tested below.

Another way to solve this problem is to assume only that  $B \rightarrow 0$  when  $r \rightarrow \infty$  faster than  $1/r$ , a condition which is reasonable in the case of solar magnetic fields. Then, direct integration of the Green's function gives the scalar potential as

$$\Phi(x, y, z) = \frac{1}{2\pi} \int \frac{B_z(x_1, y_1)}{[(x-x_1)^2 + (y-y_1)^2 + z^2]^{1/2}} dx_1 dy_1. \quad (5)$$

Here the integration is assumed to be done over an infinite plane at  $z = 0$ . In the numerical calculations, the integration is approximated by summing over a grid specified on the finite area  $S$  and this approximation is the main source of computational errors. In applying the Green's function method to the ambiguity problem, the lower boundary condition,  $B_z^{\text{obs}}$ , is approximated by the observed line-of-sight field  $B_l$ , since the vertical field is not known until the ambiguity is resolved. This is exact only at disk center, and the error in this assumption grows the further an active region is from the center of the disk. However, the Green's function method is less sensitive to the magnitude of the flux imbalance in a magnetogram than FFT-based approaches.

While determining the potential field for use in ambiguity resolution seems like a simple and straightforward problem, the many ways in which the extrapolation and the comparison can be implemented lead to significantly different results in some cases. Thus we have considered a range of implementations of the acute angle method.

In the implementation of J. Jing (NJP), the potential field extrapolation is computed using Fourier Transforms with the observed longitudinal field  $B_l$  approximating the normal  $B_z$  component as the boundary condition, strictly valid only at disk center. In this implementation, the lower boundary is periodic, not padded with zeroes, and the field of view is forced to be flux-balanced by subtracting a uniform value from the lower boundary if the flux-balance condition is not met. The acute-angle comparison is made between the transverse components of the observed field and the extrapolated field.

In the implementation of Y. Liu (YLP), the potential field was computed based on the FFT method proposed by Alissandrakis (1981). This method also assumes that the observed region is close enough to disk center so that the line-of-sight field  $B_l$  can be treated as the vertical field  $B_z$ . The acute angle test is computed for the horizontal components, that is  $\mathbf{B}_h^{\text{obs}}$  vs.  $\mathbf{B}_h^{\text{pot}}$ . No additional treatments are applied to the boundary data, that is, the lower boundary is periodic but any flux imbalance is represented by a uniform vertical field.

In the implementation of K.D. Leka (KLP), the potential field extrapolation is computed by Fourier Transform using the unambiguous line-of-sight field as the boundary condition so it does not require the observed region to be close to disk center. The area surrounding the observed field is padded with zero longitudinal field to reduce periodic effects. After an initial ambiguity resolution in the image-plane comparing the observed and computed transverse components ( $\mathbf{B}_t^{\text{obs}}$  vs.  $\mathbf{B}_t^{\text{pot}}$ ), a new potential field is computed in the heliographic plane using  $B_z$  as the boundary condition and the ambiguity is resolved by comparing the horizontal components  $\mathbf{B}_h^{\text{obs}}$  vs.  $\mathbf{B}_h^{\text{pot}}$ .

In the implementation of V. Abramenko and V. Yurchyshyn (BBP), the potential field was computed using a method based on direct integration of the Green's function (Abramenko, 1986),

$$G(x,y,z) = \frac{1}{[(x-x_1)^2 + (y-y_1)^2 + z^2]^{1/2}}, \quad (6)$$

which is smoothed over each cell of a grid and analytically corrected for the influence of sampling. In applying the Green's function method to the ambiguity problem, the lower boundary condition,  $B_z^{\text{obs}}$ , is approximated by the observed line-of-sight field  $B_l$ , since the vertical field is not known until the ambiguity is resolved. The acute-angle test is then performed between the transverse component of the observed magnetogram  $B_t^{\text{obs}}$  and the horizontal component of the potential magnetic field  $B_h^{\text{pot}}$ , again under the assumption that the region is not too far from disk center.

The implementation of J. Li (JLP) also computes the potential field using a Green's function method (Cuperman *et al.*, 1992), with some of the integrals performed analytically as described in Cuperman *et al.* (1990) in order to properly treat the singularities in the Green's function. The Green's function method approximates the vertical field with the line-of-sight field as input, but returns heliographic components of the extrapolated field, i.e. the vertical and horizontal field. The acute angle comparison is then made for transverse component of the observed and extrapolated fields.

The 180° ambiguity algorithm used at the Huairou Solar Observatory from H. N. Wang (HSO) is an acute-angle method which compares the observed field to a linear force-free field (LFFF) computed using a Fourier Transform method with the observed line-of-sight field  $B_l$  as the boundary condition (Wang, 1997; Wang *et al.*, 2001). The force-free parameter  $\alpha$  is chosen to maximize  $S$ :

$$S = \int \int P(x,y) dx dy, \quad (7)$$

where

$$P(x,y) = \frac{|\mathbf{B}^{\text{obs}} \cdot \mathbf{B}^{\text{lff}}|}{B^{\text{obs}} B^{\text{lff}}} \quad (8)$$

and  $B^{\text{obs}}$  is the observed transverse field and  $B^{\text{lff}}$  is the inferred transverse field from the linear force-free calculation. Low-signal regions are excluded from this integral.

The initial value of the force-free factor  $\alpha$  is determined according to the length scale of the field, and  $\mathbf{B}^{\text{lff}}$  is obtained with a linear force-free model using the observed line-of-sight field as the boundary condition (there is no padding with zeroes). Then the best fitting linear force-free field for  $\mathbf{B}^{\text{obs}}$  is found for the value of  $\alpha$ ,  $\alpha_{\text{best}}$ , which maximizes  $S$  in a selected window. The value of  $\alpha_{\text{best}}$  is reached by iteratively changing the value of  $\alpha$ . Finally, the azimuth in  $\mathbf{B}^{\text{obs}}$  is resolved with  $\mathbf{B}^{\text{lff}}$  using the best fitting linear force-free field and the criteria that  $\mathbf{B}^{\text{obs}} \cdot \mathbf{B}^{\text{lff}} > 0$ . The number of windows is determined according to the complexity of  $\mathbf{B}^{\text{obs}}$ . One window is enough to determine the directions of  $\mathbf{B}^{\text{obs}}$  in most solar active regions.

## 2.2. LARGE SCALE POTENTIAL METHOD

It is well established that the magnetic field in the photosphere is not force-free. A method to resolve the  $180^\circ$  ambiguity, from A. Pevtsov, utilizes two assumptions, that

- magnetograms observed with low spatial resolution can be represented quite well by force-free and even potential models.
- the deviation from non-potentiality increases with the spatial resolution.

The algorithm (LSPM) begins with a magnetogram smoothed to sufficiently low spatial resolution so as to be well-represented by the potential field. In successive iterations, the resolution is gradually increased, which introduces a gradual deviation of the azimuths' orientation from the potential field. If the resolution is increased slowly enough, the transition from the potential field to the final (possibly) non-potential field yields a smooth final azimuth that is consistent with the large scale potential field.

The method starts with a map of the observed longitudinal field, smoothed using a running boxcar filter. The size of the filter is selected to achieve a significant averaging (20-30% of the magnetogram's size). The averaged longitudinal magnetogram is used to calculate the potential field using a Fourier Transform algorithm with the area surrounding the magnetogram padded with zero longitudinal field. The observed azimuths of the transverse field are then smoothed using the same filter. The  $180^\circ$  ambiguity for the smoothed azimuths is resolved by an acute angle test between the observed and potential transverse field vectors (see Section 2.1, above). The map of the smoothed ambiguity-resolved azimuths is used as a reference for the next step: the size of a boxcar averaging filter is reduced (by about 60%), the observed map of azimuths is smoothed using this new averaging filter, and the ambiguity of the smoothed azimuths is again resolved using the acute angle requirement and the new reference.

The cycle of reducing the filter window stops when the size of a filter is equal to the pixel size of the original (observed) magnetogram. Thus, the ambiguity is first resolved with a potential field at a very coarse resolution providing a robust resolution for large-scale features. So long as the non-potential structure is re-introduced slowly, the smoothness with the previous step is maintained and the final ambiguity resolution should reflect both the large scale potential structure and the smaller scale non-potential structure of the magnetic field.

### 2.3. UNIFORM SHEAR METHOD

The Uniform Shear Method (USM; Moon *et al.*, 2003), implemented by Y. Moon, is in some ways similar to the acute angle method. However, instead of choosing the direction of the observed transverse field to be as close as possible to the corresponding potential transverse field, it is instead chosen to be as close as possible to that direction plus a constant “shear angle offset”, described below. In this manner, the method is more akin to applying the acute angle method to a linear force-free extrapolation, rather than a potential extrapolation, in that it assumes a consistent sense of twist in the field.

The USM first uses the acute angle method (Section 2.1) to resolve the ambiguity with a potential field determined using the Fourier Transform of the longitudinal field. The magnetic shear angle is then defined as the angular difference between the observed transverse field  $\mathbf{B}_t^{\text{obs}}$  and the transverse component of the potential field  $\mathbf{B}_t^{\text{pot}}$ . The uniform shear angle offset  $\Delta\theta_{\text{mp}}$  is initially estimated as the most probable value for the magnetic shear angle, assuming that the magnetic shear angle follows an approximately normal distribution. The ambiguity is resolved a second time by requiring that

$$-90^\circ + \Delta\theta_{\text{mp}} \leq \theta^{\text{obs}} - \theta^{\text{pot}} \leq 90^\circ + \Delta\theta_{\text{mp}}, \quad (9)$$

that is, that the difference between the observed transverse azimuth and the angle defined by the potential azimuth plus a constant angle offset is minimized. A second estimation of the most probable shear angle is then made by recomputing the shear and fitting a Gaussian to the histogram of the new shear angles, defining  $\Delta\theta_{\text{mp}}$  as the peak of the Gaussian, and the ambiguity resolution based on Equation (9) is repeated. The final estimate of  $\Delta\theta_{\text{mp}}$  is determined to be that which gives the maximum number of pixels in the range of  $-80^\circ + \Delta\theta_{\text{mp}} \leq \theta^{\text{obs}} - \theta^{\text{pot}} \leq 80^\circ + \Delta\theta_{\text{mp}}$  by shifting the second estimation through  $\pm 20^\circ$ . This estimate, and the resulting ambiguity resolution, aims to minimize the number of pixels with a shear angle in either tail of the histogram; it was devised to handle active regions with more complex shear angle distributions and minimizes the discontinuities in the number distribution of magnetic shear from a statistical point of view.

The final step in the method is effectively a smoothing: the observed transverse field is forced to be in the same direction as the average transverse field of the

neighboring pixels. Explicitly,

$$\mathbf{B}_t^{\text{obs}} \cdot \overline{\mathbf{B}_s^{\text{obs}}} \geq 0, \quad (10)$$

where  $\mathbf{B}_t^{\text{obs}}$  is the observed transverse field at a point, and  $\overline{\mathbf{B}_s^{\text{obs}}}$  is the mean transverse field for the surrounding area.

#### 2.4. MAGNETIC PRESSURE GRADIENT

The magnetic pressure gradient method (MPG), implemented by J. Li, is described in detail in Cuperman *et al.* (1993) (see also Harvey, 1969), but the basic underlying assumptions are that the field at the point of observation is force-free (i.e.,  $\mathbf{B} \times (\nabla \times \mathbf{B}) = 0$ ) and that the magnetic pressure decreases with height, namely,

$$\frac{\partial}{\partial z} B^2 < 0. \quad (11)$$

The force-free field assumption, along with the vanishing divergence of the field, allows the vertical derivative of the magnetic pressure to be written in terms of horizontal derivatives

$$\frac{1}{2} \frac{\partial}{\partial z} B^2 = B_x \frac{\partial B_z}{\partial x} + B_y \frac{\partial B_z}{\partial y} - B_z \left( \frac{\partial B_x}{\partial x} + \frac{\partial B_y}{\partial y} \right). \quad (12)$$

The parameters on the right hand side of the equation are observable magnetic components apart from the 180° ambiguity in the transverse fields. At disk center, the vertical field and the magnitude of the horizontal components of the field are measured, and the two choices for the direction of the horizontal component give equal magnitude but oppositely signed results for the vertical derivative of the magnetic pressure. Away from disk center, the observed line-of-sight and transverse fields can be transformed into heliographic coordinates for either choice of the ambiguity resolution, and Equation (12) still holds. In either case, the ambiguity is resolved, with no iteration, by evaluating  $\partial B^2 / \partial z$  for an initial choice of the direction of the transverse field. The direction of the transverse field is reversed at each pixel if  $\partial B^2 / \partial z > 0$  at that point.

#### 2.5. THE STRUCTURE MINIMIZATION METHOD

The structure minimization method (MS), implemented by M. Georgoulis and introduced by Georgoulis *et al.* (2004), is a semi-analytical method that eliminates inter-pixel dependencies during the disambiguation. The algorithm proceeds in two steps: an initial azimuth solution is reached analytically while the final solution is reached numerically by smoothing the initially disambiguated magnetic field vector.

The method starts by considering Ampère's law for the electric current density. Denoting the magnetic field vector as  $\mathbf{B} = B \hat{\mathbf{b}}$ , where  $B$  is the magnetic field

strength and  $\hat{\mathbf{b}}$  is the unit vector along  $\mathbf{B}$ , the electric current density  $\mathbf{J}$  is decomposed into two components, namely  $\mathbf{J} = \mathbf{J}_1 + \mathbf{J}_2$ , where

$$\mathbf{J}_1 = \frac{cB}{4\pi} \nabla \times \hat{\mathbf{b}} \quad \text{and} \quad \mathbf{J}_2 = \frac{c}{4\pi} (\nabla B) \times \hat{\mathbf{b}} . \quad (13)$$

The component  $\mathbf{J}_1$  is due to the curvature of the magnetic field lines, while the component  $\mathbf{J}_2$  is due to magnetic field gradients and is fully perpendicular to  $\mathbf{B}$  (see also the discussion in Zhang, 2001).  $\mathbf{J}_2$  is the focus for resolving the ambiguity.

For a given vector magnetogram, only the vertical component  $J_{2z}$  of  $\mathbf{J}_2$  can be readily calculated, though knowledge of the vertical gradient  $(\partial B/\partial z)$  of the magnetic field strength is sufficient for the complete determination of  $\mathbf{J}_2$ . It is assumed that the magnitude  $J_2$  of  $\mathbf{J}_2$  tends to maximize on the boundaries of magnetic flux tubes in the solar atmosphere because  $\nabla B$  maximizes in these surfaces where the transition from a magnetized to a non-magnetized medium takes place. Therefore, by minimizing  $J_2$ , the interfacing current structure between bundles of flux tubes is minimized and hence the assumption of space-filling magnetic fields in the active-region atmosphere is enforced.

The magnitude  $J_2$  is minimized when

$$\frac{\partial B}{\partial z} = \frac{b_z}{b_x^2 + b_y^2} (b_x \frac{\partial B}{\partial x} + b_y \frac{\partial B}{\partial y}) , \quad (14)$$

where  $b_x, b_y, b_z$  are the components of  $\hat{\mathbf{b}}$ . Notice that there are only two possible solutions for  $J_2$  and  $(\partial B/\partial z)$  (Equations [13] and [14], respectively), for each location, since the only differentiated quantity is the ambiguity-free magnetic field strength  $B$ . To reach the initial azimuth solution, a physical and a geometrical argument is used, namely:

- (1) it is assumed that  $(\partial B/\partial z) < 0$ , namely that the magnetic field strength decreases with height, in sunspots.
- (2) Since  $\mathbf{J}_2 \perp \mathbf{B}$ , the vector field  $\mathbf{J}_2$  must be nearly horizontal in plage, because the magnetic field  $\mathbf{B}$  is nearly vertical in these areas. Therefore, it is assumed that  $J_{2z} \simeq 0$  in plage.

The above assumptions require that sunspot and plage fields be distinguished, for which the continuum intensity is utilized. The continuum intensity,  $\omega_p$ , is normalized to fall in the range [0,1], empirically determined for the darkest umbrae and brightest strong-field regions. To reach the initial azimuth solution in the structure minimization method, we introduce a weighted function

$$\mathcal{F} = (1 - \omega_p) \frac{\partial B}{\partial z} + \omega_p |J_{2z}| , \quad (15)$$

and the azimuth solution is chosen that minimizes the magnitude of  $\mathcal{F}$  independently for every location of the magnetogram. This azimuth solution is treated as an

*initial guess* and is smoothed to provide the final solution. The type of smoothing depends on the location of the active region on the solar disk and consists of a Jacobi relaxation process applied to the initial azimuth for active regions fairly close to disk center, or pattern-recognition filtering of the initial vertical field solution for active regions far from disk center. The smoothing stops when convergence below a prescribed fractional tolerance limit is achieved for the strong-field areas of the magnetogram.

## 2.6. THE NONPOTENTIAL MAGNETIC FIELD CALCULATION METHOD

The Nonpotential Magnetic Field Calculation (NPFC; Georgoulis, 2005) method, implemented by M. Georgoulis, starts by recalling that any closed magnetic structure  $\mathbf{B}$  rooted in a surface boundary  $S$  can be represented by a potential and a nonpotential component,  $\mathbf{B}_p$  and  $\mathbf{B}_c$ , respectively, i.e.,

$$\mathbf{B} = \mathbf{B}_p + \mathbf{B}_c . \quad (16)$$

Notice that (i) all vector fields in Equation (16) are divergence-free and (ii)  $\mathbf{B}$  and  $\mathbf{B}_p$  share the same boundary condition for the vertical magnetic field  $B_z$  on  $S$ , so  $\mathbf{B}_c$  is *horizontal* on  $S$ . In addition,  $\mathbf{B}_c$  is responsible for any electric currents present since  $\mathbf{B}_p$  is current-free. From these conditions, and the further assumption that  $\partial B_{c_z}/\partial z$  vanishes on the boundary  $S$ , the nonpotential field  $\mathbf{B}_c$  becomes analytically determined on  $S$  in terms of the vertical electric current density by

$$\mathbf{B}_c = \mathcal{F}^{-1} \left[ \frac{ik_y}{k_x^2 + k_y^2} \mathcal{F}(j_z) \right] \hat{\mathbf{x}} + \mathcal{F}^{-1} \left[ \frac{-ik_x}{k_x^2 + k_y^2} \mathcal{F}(j_z) \right] \hat{\mathbf{y}} \quad (17)$$

where  $\mathcal{F}(r)$  and  $\mathcal{F}^{-1}(r)$  are the direct and inverse Fourier transforms of  $r$ , respectively, and  $j_z = 4\pi J_z/c$ . The condition that  $\partial B_{c_z}/\partial z$  vanish on  $S$  is equivalent to assuming that  $\partial B_z/\partial z = \partial B_{p_z}/\partial z$  on  $S$ , i.e. that the vertical derivative of  $B_z$  is given by the vertical derivative of the vertical potential field.

After calculating  $\mathbf{B}_c$ , the disambiguation problem requires finding the distribution  $B_z$  of the vertical magnetic field whose potential extrapolation  $\mathbf{B}_p$  plus the calculated nonpotential field  $\mathbf{B}_c$  (Equation [16]) best matches the observed heliographic horizontal magnetic field. This is achieved iteratively, and provides the azimuthal resolution.

Therefore, the problem is to find the vertical current density  $J_z$ , or a good proxy of it, *prior* to the disambiguation. Georgoulis (2005) used an ambiguity-free proxy of  $J_z$  derived by extracting from the longitudinal magnetic field  $B_l$  any information on the heliographic horizontal field present in  $B_l$  due to projection effects. Specifically, the average of the two possible heliographic ambiguity solutions,  $\mathbf{B}_{av} = (1/2)(\mathbf{B}_1 + \mathbf{B}_2)$ , depends only on  $B_l$ , i.e.  $\mathbf{B}_{av} = \Gamma B_l$ , where  $\Gamma$  is a known vector field depending on the direction cosines of the heliographic transformation. Then, a proxy for vertical current density  $J'_{z_p}$  is constructed by applying Ampère's

law to  $\mathbf{B}_{av}$ . The calculation of  $J'_{z_p}$  is done once, at the beginning of the iterative process for  $B_z$ , and the resulting nonpotential field  $\mathbf{B}_c$  is fixed and used in each iteration. The magnitude of  $J'_{z_p}$  depends on the observing angle to the active region, since the extent of the projection effects on  $B_l$  depends on the location of the measurements. On or close to disk center,  $J'_{z_p} \simeq 0$ , so the resulting  $\mathbf{B}_c \simeq 0$ . In this case, the NPFC method degenerates to a simple potential field acute angle method.

### 2.6.1. Recent Improvements

The calculation of the proxy current density in the NPFC method has been improved over that described above (Georgoulis, 2005), effectively in response to discussions at the NCAR workshop, and the results of this new approach are presented here (NPFC2)<sup>1</sup>. The proxy vertical current density  $J_{z_p}$  is now updated at each iteration  $i$  by applying Ampère's law to the interim resolved magnetic field vector, i.e.,  $(4\pi/c)J_{z_p}^{(i)} = [\nabla \times \mathbf{B}^{(i)}]_z$ . Very large values of  $J_{z_p}^{(i)}$  imply azimuth discontinuities, and are set to zero in order not to affect the calculation of  $\mathbf{B}_c$ . The seed current density  $J_{z_p}^{(0)}$  at the beginning of the iterations uses  $J'_{z_p}$  as in Georgoulis (2005) but also employs the parity-free absolute vertical current density derived by Semel and Skumanich (1998) in the form

$$J_{z_p}^{(0)} = s(J'_{z_p})[\sin^2 L |J'_{z_p}| + \cos^2 L |J_{z_{SS}}|] . \quad (18)$$

In Equation (18),  $s(J'_{z_p})$  is the sign of  $J'_{z_p}$ ,  $|J_{z_{SS}}|$  is the expression of Semel and Skumanich (1998) calculated using the line-of-sight magnetic field components, and  $L$  is the heliographic longitude of the location where  $J_{z_p}^{(0)}$  is calculated. On or close to disk center, the major contribution to  $J_{z_p}^{(0)}$  comes from  $|J_{z_{SS}}|$  which roughly corresponds to the true magnitude of the vertical current density. Far from disk center,  $J_{z_p}^{(0)}$  stems mostly from  $J'_{z_p}$  which is a lower limit of the true heliographic current.

An additional change is that the field of view in the NPFC method is now padded with zeroes to mitigate periodic boundaries in the Fast Fourier Transforms in calculating  $\mathbf{B}_p$  and  $\mathbf{B}_c$ . When the field of view contains a flux-imbalanced magnetic structure or when strong magnetic flux resides on or close to the boundaries of the field of view it is often helpful to place a mirror of the actual image on the extensions which are normally padded with zeroes. This mirroring is done, for example, with test case #1 described below.

The convergence is tested by means of the number of vector flips or, equivalently, the number of flipped  $B_z$ -values in each iteration for strong-field locations. The convergence test in the initial NPFC is the one described in Georgoulis (2005) namely a fractional tolerance limit for  $B_z$  over the field of view. The number of flips is introduced in the revised NPFC because it is a more readily implemented and easily understood criterion.

<sup>1</sup> Code is available at [http://sd-www.jhuapl.edu/FlareGenesis/Team/Manolis/codes/ambiguity\\_resolution/](http://sd-www.jhuapl.edu/FlareGenesis/Team/Manolis/codes/ambiguity_resolution/)

## 2.7. PSEUDO-CURRENT METHOD

The pseudo-current method (PCM; Gary and Démoulin, 1995), implemented by G. A. Gary, resolves the  $180^\circ$  ambiguity by minimizing the square of the vertical currents of the observed vector magnetogram. The ambiguity is first resolved using the potential field acute angle rule (see Section 2.1) to determine an initial vertical electric current density,  $J_z$ . The transverse potential field is computed via an Alissandrakis FFT approach using the line-of-sight corrections, i.e. correcting for off-disk center viewing, with boundary buffering equivalent to the FOV. Subsequently,  $N$  major local maxima of  $|J_z|$  are used to locate the positions  $\mathbf{R}_i = (x_i, y_i)$ ,  $i = 1, \dots, N$  of different “sources” of nonpotentiality.

Each source is used to define an individual  $J_z$  patch ( $\tilde{J}_{zi}$ ) that is taken as a radially symmetric function to allow analytical integration. The current within each patch is defined by

$$\tilde{J}_{zi}(\mathbf{r}, p_i) = \frac{\tilde{J}_{zi}^{\max}}{2} \left[ \cos \left( \frac{\pi}{\rho_i} |\mathbf{r} - \mathbf{R}_i| \right) + 1 \right], \quad |\mathbf{r} - \mathbf{R}_i| \leq \rho_i. \quad (19)$$

A reference field is generated by using these patches to define vertical line currents and adding the resultant ad hoc magnetic field to the potential field. The parameters of the reference field are  $p_i = \{x_i, y_i, \tilde{J}_{zi}^{\max}, \rho_i\}$ , where  $\tilde{J}_{zi}^{\max}$  is the maximum current density of the patch and  $\rho_i$  is the characteristic radius. The reference transverse field is used to resolve the ambiguity of the observed field using the acute angle rule. The parameters are then allowed to vary and the functional,

$$F[J_z^2] = \int \int J_z^2(x, y, p) dx dy. \quad (20)$$

is minimized with respect to the set of parameters,  $\{p_i\}$ , using a multidimensional conjugate gradient method.

## 2.8. U. HAWAI‘I ITERATIVE METHOD

The group at U. Hawai‘i Institute for Astronomy developed an automated iterative method (UHIM; Canfield *et al.*, 1993) which (1) performs an initial “acute-angle” resolution based on a potential field calculated via FFT from the observed line-of-sight field,  $\mathbf{B}_l$ , comparing  $\mathbf{B}_l^{\text{obs}}$  vs.  $\mathbf{B}_l^{\text{pot}}$  (see Section 2.1) (2) uses the resulting vertical field,  $\mathbf{B}_z$ , to perform a refining “acute-angle” resolution based on a constant- $\alpha$  force-free field with a specified  $\alpha$ , (3) starting from a radial point, e.g. a sunspot umbra, “smooths” by minimizing the angle between each pixel and its neighbors, and, finally, (4) minimizes  $|J_z|$  or  $|\nabla \cdot \mathbf{B}|$  according to a specified threshold for the transverse magnetic field,  $B_t$ ; for the latter,  $\partial B_z / \partial z$  is determined from the constant- $\alpha$  force-free field.<sup>2</sup>

<sup>2</sup> Code is available at [http://www.cora.nwra.com/AMBIGUITY\\_WORKSHOP/CODES/mgram.tar](http://www.cora.nwra.com/AMBIGUITY_WORKSHOP/CODES/mgram.tar)

The code, written in the IDL language and implemented here by K.D. Leka, includes numerous keywords which govern its operation. Examples of the parameters that can be set by the operator include the force-free parameter  $\alpha$  with which to compute a force-free field and the minimization threshold alluded to above. Although there are nominal default values, in practice inputs such as  $\alpha$  are either derived from the data itself or specified by the user, depending on the level of autonomy required. While the large number of keywords allows for significant flexibility, this approach also provides repeatability. The code is part of a code-tree which includes a program that computes a best-fit  $\alpha$ , selected by minimizing the difference between the transverse components of the observed field and the linear force-free field (Leka and Skumanich, 1999; Pevtsov *et al.*, 1995).

Since the method was initially described (Canfield *et al.*, 1993), various improvements have been made. Most importantly, for the results presented here, the minimization was performed based on  $J_z^2$  rather than  $|J_z|$ ; this results in fewer “line currents” forming, where conflicting regions of resolution preference “collided” resulting in a line of discontinuity separating two smooth solutions.

Ultimately, it is the minimization of  $J_z^2$  and  $|\nabla \cdot \mathbf{B}|$  which resolves the ambiguity, but, since the space of possible solutions is huge, the prior steps are designed to bring the solution close to the correct solution so that the fast, iterative minimization avoids local minima.

## 2.9. MINIMUM ENERGY METHODS

The “minimum energy” algorithm (ME1; Metcalf, 1994), implemented by T. Metcalf, simultaneously minimizes both the electric current density,  $J$ , and the field divergence. Minimizing  $|\nabla \cdot \mathbf{B}|$  gives a physically meaningful solution and minimizing  $J$  provides a smoothness constraint. It was shown by Aly (1988) that, for a force-free field, the magnetic free energy is bounded above by a value proportional to the maximum value of  $J^2/B^2$ . Since  $B^2$  is unambiguous, by minimizing  $J^2$  we are minimizing the upper bound on the magnetic free energy. It is in this sense that this method is a “minimum energy” algorithm.

The algorithm used here is almost the same as the one described by Metcalf (1994), but one change has been made: the functional to be minimized,  $E = \sum (|\nabla \cdot \mathbf{B}| + |J|)$ , has been replaced by  $E = \sum (|\nabla \cdot \mathbf{B}| + |J|)^2$ . Squaring the pseudo-energy function has the advantage that more spread out currents are favored over line currents, as discussed in the previous section for the UH Iterative method.

The calculation of the vertical electric current density,  $J_z$ , is straightforward, requiring only observed quantities in the computation and a choice of the ambiguity resolution. However, calculation of  $\nabla \cdot \mathbf{B}$  and the horizontal current,  $J_x$  and  $J_y$ , requires a knowledge of the vertical derivatives of the magnetic field. Variations of the magnetic field with height are not normally known (but see Leka and Metcalf, 2003), so the vertical derivatives of the field are approximated with a linear force-free field (LFFF) extrapolation using the unambiguous line-of-sight field as the

lower boundary condition. The force-free parameter,  $\alpha$ , is computed in the same manner as described above in Section 2.8.

Since the calculation of  $J$  and  $\nabla \cdot \mathbf{B}$  involves derivatives of the magnetic field, the computation is not local and the number of possible solutions is huge ( $2^N$ , where  $N$  is the number of pixels; a local algorithm would have only  $2N$  possibilities). Further, the solution space has many local minima. Hence, the “simulated annealing” algorithm (Metropolis *et al.*, 1953; Kirkpatrick *et al.*, 1983) is used to find the global minimum, an extremely robust approach when faced with a large, discrete problem (there are two and only two possibilities at each pixel) with many local minima (Metcalf, 1994).

### 2.9.1. *Recent Improvements*

The minimum energy approach depends on a linear force-free extrapolation to derive the height dependence of the field. Since the  $180^\circ$  ambiguity presents us with two very different choices at each pixel, the approximate height dependence of the field computed from the constant  $\alpha$  extrapolation is often adequate.

However, it is well known that  $\alpha$  is far from constant in typical solar active regions (Leka, 1999; Pevtsov *et al.*, 1994). Hence a modification to the original approach has been implemented, the “non-linear minimum energy method” (ME2), which partially relaxes the constant  $\alpha$  assumption. While it would be ideal to use a full non-linear force-free field (NLFFF) extrapolation to derive the vertical field structure, this is too slow given today’s computing resources. Hence, we apply the above minimum energy algorithm *locally* within the magnetogram. The magnetogram is divided into a number of overlapping tiles; the best value of the linear force-free  $\alpha$  is then computed separately for each tile, in effect allowing  $\alpha$  to vary over the field of view. A LFFF extrapolation is computed over the full field-of-view for each value of  $\alpha$ , and the height dependence of the magnetic field is taken for each tile from the LFFF extrapolation with the value of  $\alpha$  appropriate for that tile. That is, a map of the vertical structure of the field is constructed from these tiles for which  $J_x$ ,  $J_y$  and  $\partial B_z / \partial z$  are computed for the full magnetogram. The algorithm then proceeds as above using simulated annealing to minimize  $E = \sum (|\nabla \cdot \mathbf{B}| + |J|)^2$ .

## 2.10. THE HAO AZAM UTILITY

As part of the software developed for the HAO/NSO Advanced Stokes Polarimeter (Elmore *et al.*, 1992), the utility “AZAM”, was developed in IDL for the interactive resolution of the azimuth ambiguity. In addition to ambiguity resolution, it can display the vector field results in a variety of ways. AZAM has a common goal with methods that minimize both the current (by imposing smoothness) and an approximation to the divergence (by matching expectations of solar structure).

In simple terms, AZAM, implemented here by B. Lites, allows the user to interactively “mouse-over”, or “paint”, azimuth choices in either the observer’s or the

local solar reference frame. Within a chosen pixel sub-area (ranging from  $2 \times 2$  to  $16 \times 16$  pixels in powers of 2), it sets the selection of ambiguity according to one of a variety of rules. One such rule, used here, chooses the azimuth such that all points within the sub-area have an azimuth resolution closest to their nearest neighbors. For the  $2 \times 2$  case, it selects the solution with the maximum sum of the dot products of the transverse field at neighboring pixels in the cardinal directions. For larger sub-areas, it starts by breaking the sub-area down into  $2 \times 2$  blocks, maximizes the sum of the neighboring pixel dot products within each block, then scales up by factors of 2 until reaching the full size of the sub-area.

By “mousing-over” the image, one may set the ambiguity resolution to minimize local discontinuities, although this does not necessarily produce the minimum magnitude of the vertical current density within a chosen pixel sub-area. AZAM allows a variety of initial guesses, including the closest resolution to a potential (current free) field solution. Furthermore, it is possible to apply a local smoothing over the whole image to minimize discontinuities. One typically starts the interactive resolution from the centers of unipolar sunspot umbrae where the horizontal field must diverge (converge) away from the center of the umbra for positive (negative) polarity. This sets the ambiguity resolution locally, and one typically works outward from the sunspot centers. The solution is deemed to have been reached when the operator is satisfied with the results.

### 3. Comparisons

To test the performance of the algorithms, we must have data sets for which the correct ambiguity resolution is known. Presently, the only ways to obtain such data sets are from MHD simulations, or from analytic solutions to the MHD equations. After applying the algorithms to these data sets, we must have quantitative means for assessing their performance. Here we outline the two data sets used, the metrics devised, and, finally, discuss the results for each of the algorithms.

#### 3.1. THE HARES

For this experiment, two “hares” were used, selected to challenge the algorithms with various aspects of solar active regions known to be problematic for resolving the ambiguity in observational data. However, in both cases, the solution is provided on a grid that is sufficiently fine to resolve all the structure in the magnetic field, but the number of grid points is small enough that no smoothing or interpolating is required by any of the methods except the LSPM. Thus no attempt is made to investigate the sensitivity of the methods to issues of spatial resolution.

##### 3.1.1. *Case #1: Twisted Fluxrope in a Potential-Field Arcade, $\mu = 1.0$*

The first test case is a “photospheric” vector magnetogram constructed from the MHD model of Fan and Gibson (Fan and Gibson (2003); Fan and Gibson (2004)),

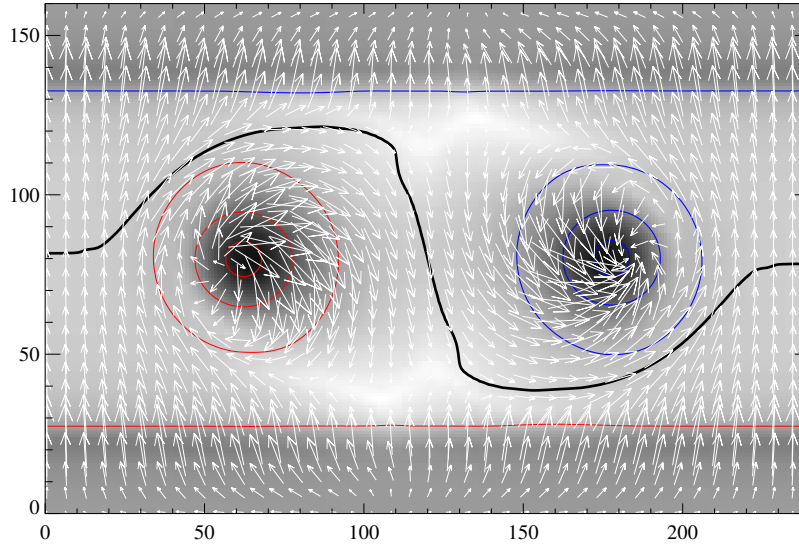


*Figure 1.* Vector magnetic field at  $z = 0.006L$  from the numerical simulation of Fan and Gibson (2004), at their timestep 56. Underlying “continuum image” is a reverse-color image of  $B^2$ ; positive/negative vertical magnetic flux is indicated by red/blue contours at 100, 1000, 2000 G, and the magnetic neutral line is also indicated by the black contour. Horizontal magnetic field is plotted at every 5th pixel, with magnitude proportional to arrow length. Tickmarks are in units of pixels.

provided courtesy of Y. Fan. The simulation emerged a twisted magnetic flux rope, with approximately constant force-free parameter  $\alpha$  into an overlying potential “arcade” field. A “snapshot” at time-step 56 was the source of the boundary field, at  $z = 0.006L$  ( $L$  is the length scale for the model, effectively the box-length in the  $\hat{y}$  direction), or slightly above the lower surface (see Figure 1). At this layer the field is forced (Fan and Gibson, 2004; Leka *et al.*, 2005) but continuous; relevant factors for this project are that it appeared at “disk center” such that  $B_l = B_z$  on a grid of  $240 \times 160$  pixels, each  $1.0''^2$ , and the magnetic neutral line included a “bald patch” (Gibson *et al.*, 2004), where the horizontal field traverses the magnetic neutral line from negative to positive polarity. Additionally, the presence of both the flux-rope footpoints and the arcade meant that this magnetogram included both potential fields and regions that were forced (i.e.  $\mathbf{J} \times \mathbf{B} \neq \mathbf{0}$ ) and hence far from potential. Finally, the simulation used perfectly conducting side walls, so that no field lines could escape from the edges of the box.

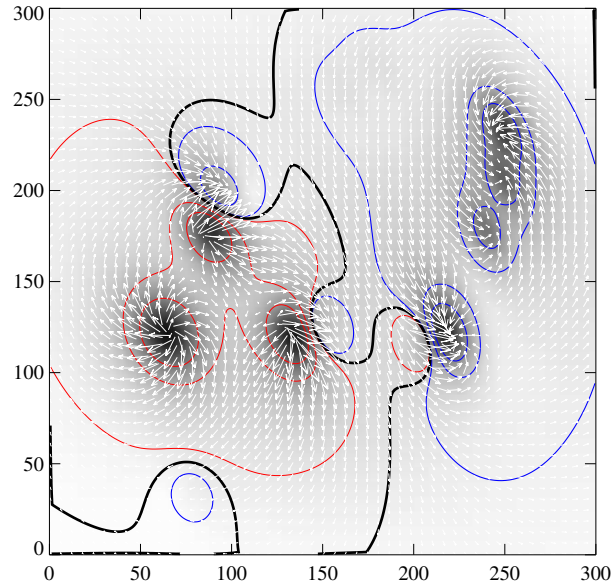


*Figure 2.* Vector magnetic field for the multi-polar structure in image coordinates. Underlying “continuum image” is a reverse-color image of  $B^2$ ; positive/negative vertical magnetic flux is indicated by red/blue contours at 100, 1000, 2000 G, and the magnetic neutral lines are also indicated by the black contour. Horizontal magnetic field is plotted at every 5th pixel. Tickmarks are in units of pixels.

### 3.1.2. Case #2: Multi-polar constant- $\alpha$ Structure, $\mu \neq 1.0$

The second test case is a “chromospheric” vector magnetogram constructed from a collection of point sources located on a plane below the surface. The contribution to the field of each source is calculated using the Green’s function given by Chiu and Hilton (1977) with a constant value of the force-free parameter  $\alpha$ . The use of a single value for  $\alpha$  means that the field is everywhere force-free. Four of the sources are distributed according to the discussion in Titov *et al.* (1993) to produce a “bald patch” along part of the neutral line. A number of additional sources are used to produce a distribution of flux that has the appearance of an active region (Figure 2).

Although the net charge of all the sources vanishes, one of the sources is placed outside of the field of view, so the resulting magnetogram is not flux balanced, as is typical for a real vector magnetogram. The field is then calculated on a regular grid of  $300 \times 0.5''^2$  in the image plane, with the center of the field of view at effectively N  $18^\circ$ , W  $45^\circ$ , so that the line-of-sight field is distinctly different from the normal component of the field.

### 3.2. THE METRICS

For a quantitative comparison of the methods described above, various metrics,  $\mathcal{M}$ , were employed which highlighted the successes and failures in different ways. For each, the “solution” provides an azimuth choice  $\theta_s$  which is compared to the “answer”’s azimuth choice  $\theta_a$ , all in the image (or “instrument” or “observer”) plane resulting in a map of  $\Delta\theta$  that will be either  $0^\circ$  or  $\pm 180^\circ$ . The metrics were computed according to this map and the field (where relevant) obtained from the “answer” data file. The metrics we adopted are:

- **Area:** a simple fraction of pixels where the submitted solution agreed with the answer:  $\mathcal{M}_{\text{area}} = \#\text{pixels}(\Delta\theta = 0) / \#\text{pixels}$ . “Good” is closer to 1.00; “random” would give 0.50.
- **Flux:** The fraction of the magnetic flux, computed using the answer’s  $B_z$ , where  $\Delta\theta = 0$ :  $\mathcal{M}_{\text{flux}} = \sum(|B_z|_{\Delta\theta=0}) / \sum(|B_z|)$ . Again, “good” is closer to 1.00; “random” would give 0.50.
- **Strong Horizontal Field:** The fraction of strong horizontal magnetic field which was correctly resolved. Both model field test cases were scaled similarly with regards to field strengths in the “spots”, etc. and a threshold of 500 G for the horizontal was adopted above which  $B_h$  was considered strong. Then, calling this strong-horizontal-field  $B_h(s)$ , this metric is computed as  $\mathcal{M}_{B_h(s)} = \sum(B_h(s)_{\Delta\theta=0}) / \sum(B_h(s))$ , and again, “good” is closer to 1.00; “random” would give 0.50.
- **Vertical Current:** In a different approach, the vertical currents were computed for both the submitted solutions and the answer, and compared. In this metric, the solution is rewarded where it is correct *and* penalized where it is incorrect:

$$\mathcal{M}_{J_z} = 1 - \frac{\sum(|J_z(\text{answer}) - J_z(\text{solution})|)}{2\sum(|J_z(\text{answer})|)}. \quad (21)$$

$\mathcal{M}_{J_z}$  has been constructed such that “good” is still closer to 1.00, and normalized such that a value of 0.00 would occur if the current were exactly reversed at each pixel; scores less than 0.00 indicate the presence of strong line currents. A score of about 0.00 can also be attained with a combination of exactly reversed currents and moderate line currents.

### 3.3. THE RESULTS

The results are shown in Table II, and Figures 3 and 4. Below, we summarize how each method performed, highlighting the strengths and the weaknesses of each.

The acute angle methods make a useful benchmark for comparison with other methods. They are fast, automatic, and simple to implement. To add value, the more

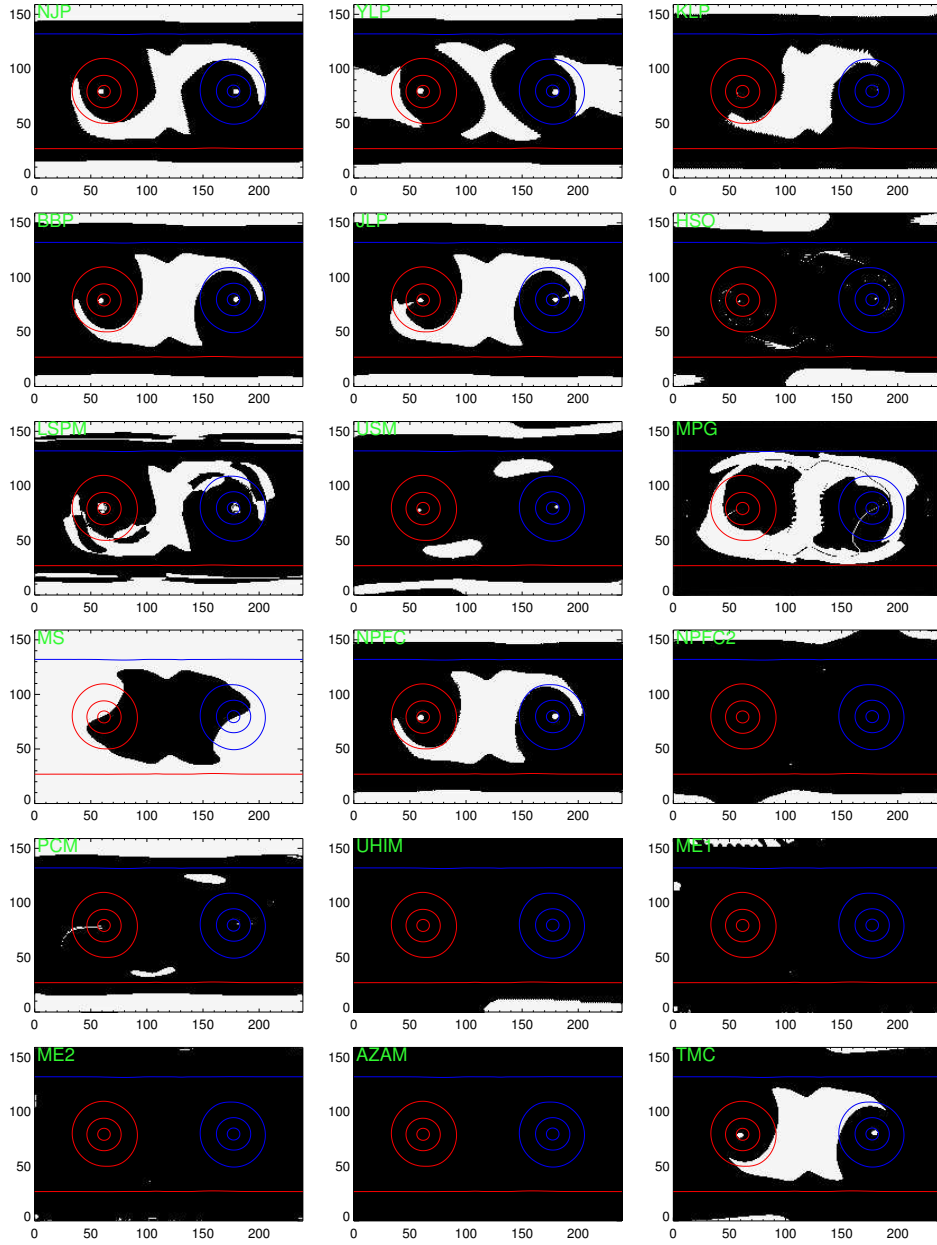


Figure 3. Results for Case #1, the emerging fluxrope simulation of Fan and Gibson (2004), at timestep 56. Contours are the same as Figure 1 for reference. Areas with the correct ambiguity resolution are black, incorrect areas are white. Figures are in the order that the descriptions appear in the text, and labeled with an acronym (see Table II) to help identification.

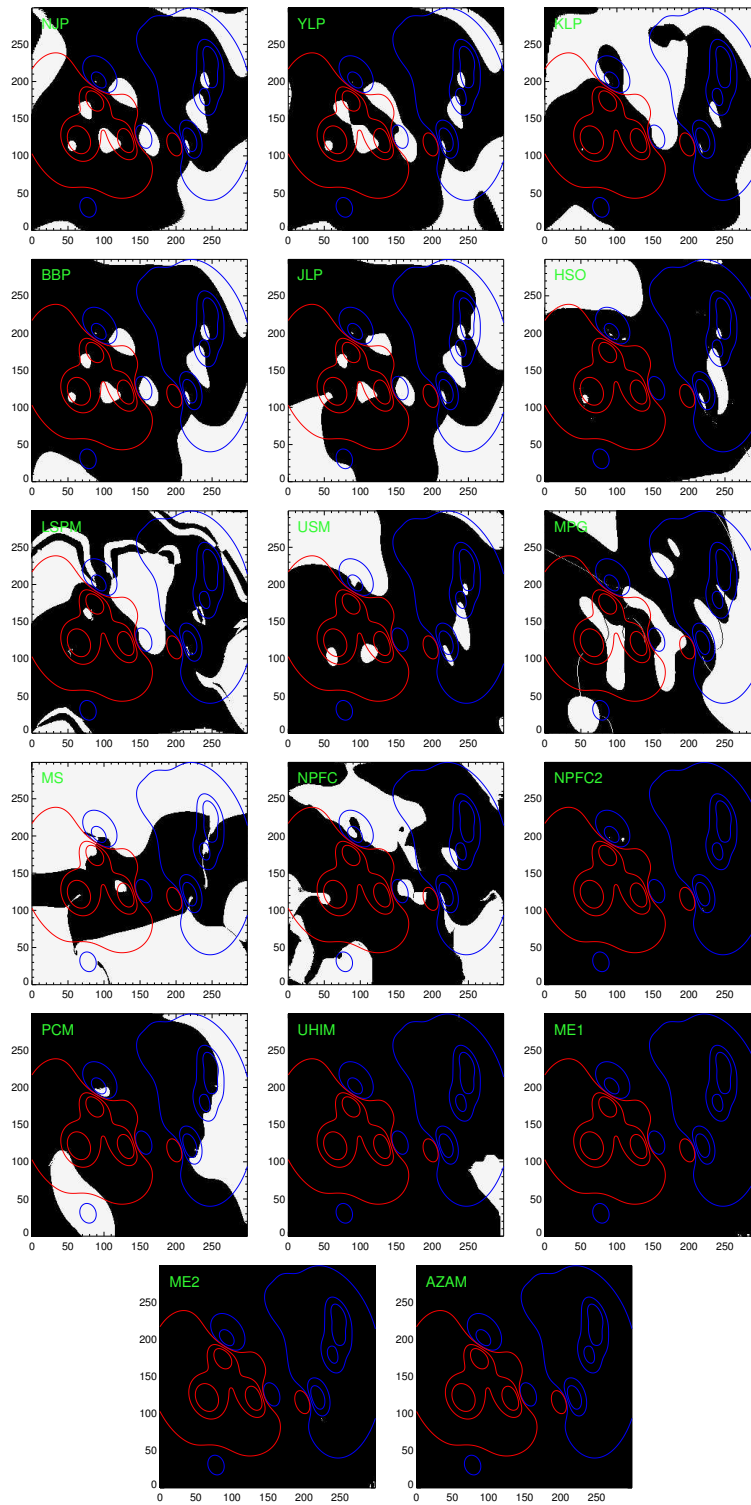


Figure 4. Results for Case #2, the multipoles positioned away from disk center. Presentation is the same as Figure 3, with the contours from Figure 2 included for reference.

complex algorithms need to perform better than the acute angle techniques. If they do not, there is nothing gained by implementing the more complex algorithms.

None of the acute angle methods scores particularly well on either of the test cases. For the potential field methods, the scores on all the metrics fall in the range  $0.6 \lesssim \mathcal{M} \lesssim 0.9$  except for the current metric, which is significantly worse at  $-0.1 \lesssim \mathcal{M}_z \lesssim 0.25$ . Perhaps the most interesting feature was the wide variation in the scores of the various implementations. Qualitatively, the methods all had difficulties in the same areas for the flux rope simulation: the arcade field and a band centered between the footpoints of the flux rope. For the arcade field, it is not surprising that the methods all had difficulties: the side walls of the simulation were perfectly conducting, so field lines were prevented from leaving the box, whereas the various implementations of the potential field method had periodic boundary conditions (Fourier Transform methods) or open boundary conditions (Green's function methods), so field lines from the arcade could leave the sides of the box. Given knowledge of the side wall boundary conditions, the potential field extrapolation could be improved for the arcade.

We have tested this through a modification of the potential field acute angle algorithm (labeled TMC in Figure 3 and Table II). By reflecting the lower boundary about the side walls before applying the Fourier Transform method in the computation of the potential field, the perfectly conducting walls of the arcade field are simulated. The resulting potential field is used to resolve the ambiguity using the acute angle algorithm. The result is much improved at the top and bottom edges since the boundary conditions now match those applied in the computation of the arcade field, i.e. no field lines are allowed to leave the box through the side walls. The scores are now  $\mathcal{M} > 0.83$  for the first three metrics, and  $\mathcal{M}_z = 0.39$ . This exercise demonstrates the sensitivity of the acute angle algorithms to the particular implementation of the boundary conditions. Of course, if one knows the true side wall boundary conditions, it would be helpful to many of the methods, but, in real solar cases, one does not have this information.

The other area in which the potential field methods had difficulty is part of the area of highly-nonpotential field in the flux rope. The “bad” part does not follow the neutral line between the foot points of the flux rope, but it does encompass the bald patch section. This is not surprising, because this is the section in which the horizontal field is directed from negative polarity to positive polarity, i.e., “backwards”. While such an orientation is possible with a potential field, it requires special circumstances (Titov *et al.*, 1993). What is perhaps surprising is that the centers of the foot points of the flux rope are mainly reproduced correctly, so the majority of the flux in the flux rope is correct. The exact area in which the acute angle method was successful depended on the implementation of the potential field extrapolation. This indicates the sensitivity of the acute angle method: a small change in the potential field can result in a different choice of azimuth over a significant area. It was interesting to note, however, that potential field methods were correct for some regions in which currents were present, and failed in some regions in which

the field truly was potential. Using a linear force-free extrapolation instead of a potential field resulted in scores in the same range except on the current metric, which improved significantly to  $0.6 \lesssim \mathcal{M}_{J_z} \lesssim 0.7$ .

The Large Scale Potential Method has difficulties in the same general areas as the acute angle methods, with one distinct difference: it does not obtain a smooth solution. There are narrow bands in which the solution flips from correct to incorrect. In some cases, this may improve the area in which the solution is correct slightly, but it comes with a large cost: strong line currents are introduced where the solution flips. This results in the much worse scores of  $\mathcal{M}_{J_z} = -0.84$  (Case #1) and  $\mathcal{M}_{J_z} = -0.38$  (Case #2), in comparison to the acute angle methods. On the plus side, this algorithm is computationally fast and might be appropriate for automated processing of “quick-look” data.

The Uniform Shear Method performed very similarly to the linear force-free field acute angle algorithm, both in the scores, with  $\mathcal{M} \gtrsim 0.65$  for all the metrics except  $0.4 \lesssim \mathcal{M}_{J_z} \lesssim 0.5$ , and in the areas in which it failed. This is not surprising since the algorithm assumes a constant shear offset over the full magnetogram; this does not necessarily result in a constant force-free parameter, but it does indicate a similar consistent twisting of the field. Unless the field of view contains only a single flux tube, it is likely that the distribution of shear angles will not resemble a Gaussian, and indeed may not be unimodal, hence the uniform shear method is best applied locally, for example along a single sheared neutral line, where the magnitude and sign of the shear is more consistent. This is confirmed by the success of the method along the bald patch in Case #1, and by the high scores on the horizontal field metric ( $\mathcal{M}_{B_h(s)} \gtrsim 0.9$ ) in both cases.

The Magnetic Pressure Gradient algorithm assumes that the magnetic pressure is decreasing with height. While this is correct over much of the test cases, it is incorrect in some important areas. For example, the magnetic field over bald patches increases with height (Titov *et al.*, 1993), and the method did indeed fail in the vicinity of the bald patches in both test cases. That this algorithm is based on an (occasionally) incorrect assumption may explain why the algorithm did not score noticeably better than the potential field acute angle algorithms.

The minimum structure algorithm performed poorly on both test cases, and was worse than a random selection in Case #1, with  $\mathcal{M} < 0.3$  for all metrics. Although the method is computationally fast, the disambiguation relies on the validity of the minimum structure approximation (Equation [14]) as well as additional assumptions that may break down locally. For example, the assumption  $(\partial B / \partial z) < 0$  in sunspots is not always correct (Leka and Metcalf, 2003), and the method refers specifically to sunspot and plage fields, thus misrepresenting other structures such as canopies or emerging flux regions. We hypothesize that for Case #1 which simulated an emerging flux region, the assumptions were simply not applicable. For Case #2, the continuum intensity was modeled as proportional to  $1 - B^2 / (2B_{\max}^2)$ , so the method may have been misled in identifying spots and plage. In addition,

the final smoothing is a numerical necessity dictated by the imperfections of these assumptions and lacks a solid physical background.

It is interesting to compare the Magnetic Pressure method to the Minimum Structure method, as both take the same approach in regions of strong field (sunspots). However, even in strong field regions, there are large areas where the two obtain different results, indicating the large role that the smoothing plays in the Minimum Structure method.

The NPFC algorithm is represented both by results from the original algorithm (Georgoulis, 2005), and the modified version described above. The original algorithm did not score better than the acute angle algorithms, however, the modified version scored significantly better, with  $\mathcal{M} \gtrsim 0.8$  for Case #1 and  $\mathcal{M} \gtrsim 0.98$  for Case #2. The improvement can likely be attributed to the more robust estimation of  $J_z$  and its iterative updates. In Case #1, which was exactly at disk center, the original version of the NPFC algorithm reduced to a potential field ambiguity resolution because  $J'_{z_p} = 0$  from symmetry. The NPFC algorithms are reasonably fast and fully automated.

The Pseudo-Current algorithm performed reasonably well in each test, typically with  $\mathcal{M} \approx 0.8$ . However,  $\mathcal{M}_{J_z} \approx 0.5$ , which was similar to the LFFF acute angle method and significantly higher than the typical values around 0.0 for the potential field acute angle methods. This algorithm is suited for highly nonpotential magnetic field regions, cases where the potential field algorithm fails, as again distinguished by the  $\mathcal{M}_{J_z}$  metric. The algorithm is local in nature, hence it is fast, automated, and independent of the field of view of the magnetogram. Its goal is similar to that of the minimum energy solutions, with an optimization scheme that is fast but, in general, unable to guarantee a global minimum. In addition, the method had difficulty with the arcade field in Case #1, likely for the same reasons that the potential field methods failed here: the perfectly conducting walls.

The UH Iterative algorithm scored significantly better for all cases than the various acute-angle methods, with  $\mathcal{M} \gtrsim 0.88$  for all metrics in Case #1 and  $\mathcal{M} \gtrsim 0.97$  in Case #2; it scored significantly better for both cases than the other algorithms highlighted thus-far and was comparable to the revised NPFC. It had fewer difficulties with the arcade field in Case #1, indicating that it is less sensitive to the potential field extrapolation. This iterative minimization can be classified as “reasonably fast” and fully automated; as such, it may be very appropriate when there is a need to balance speed and accuracy.

The two “minimum energy” algorithms scored extremely well for both test cases, on all metrics. The minimum energy and non-linear minimum energy methods had  $\mathcal{M} \gtrsim 0.99$  for each metric on Case #2, while the original implementation had some minor difficulties with Case #1, resulting in a lowest score of  $\mathcal{M}_{J_z} = 0.93$ . The few pixels that were not treated correctly were at the edge of the field of view where boundary problems in computing  $\nabla \cdot \mathbf{B}$  appear. Both of these minimum energy approaches are fully automated, but can be classified as slow (minimum

energy) and very slow (non-linear minimum energy). As such, they may be best suited for magnetograms undergoing detailed analysis.

The AZAM utility was able to successfully recover the correct azimuth for essentially every pixel in both test cases, resulting in scores that, for all cases, were 1.0. The test cases have a continuous, smooth variation of the field vector over the simulated field. Because of this, they represent an almost trivial case for AZAM since, if one is able to select the correct ambiguity resolution at one point in the field, AZAM will lead to the correct resolution at every other point by working outward from the first point. It is therefore not obvious in the case of spatially discontinuous data, for example as is generally presented by observations, that AZAM will perform better than other methods.

A particular advantage of AZAM is that one can manually incorporate other information that may be helpful for tricky ambiguity resolution problems. Sometimes active regions require that the choice of azimuth include a discontinuity between nearest neighbors: that is, there must be a place where the adjacent pixel has an azimuth that is not the selection closest to that of the current pixel. AZAM interactively displays the locations of these discontinuities, and allows one to use other information (such as abrupt changes in the intrinsic field strength) to “push” the discontinuity to locations where it makes some physical sense; i.e. where a larger shift in azimuth might be acceptable. The flexibility of AZAM to display different quantities such as the intrinsic field strength, along side of the azimuth and inclination, are powerful advantages of this method.

Presently, AZAM is not written in a way that is easily adapted to data from other sources, but this update is planned as part of the NCAR Community Spectropolarimetric Analysis Center (CSAC). Being a manual method, one must become familiar with its usage. Use of AZAM thus remains somewhat of a learned art rather than a method based on well-defined physical principles. Furthermore, since it requires human intervention, it is impractical to use AZAM as a routine method for resolving the ambiguity in upcoming missions, such as Solar-B and SDO. Finally, it is almost impossible for one user to exactly duplicate the ambiguity resolution of another user for solar data. However, it is likely that AZAM, or some derivative, may remain useful in the future as a procedure to impose final conditioning upon results from automatic azimuth ambiguity resolution procedures, especially for active regions that have highly sheared and non-potential features.

#### 4. Summary and Conclusions

Today’s measurements of the solar magnetic field most commonly comprise spectropolarimetric data, from which single-height maps of the  $180^\circ$  ambiguous vector are derived. In order to resolve the ambiguity and obtain physically meaningful data, *some* assumption must be made about the solar field. Typically, this assumption involves minimizing a quantity which itself depends on the choice of azimuth.

Despite the array of methods presented here, the number of quantities chosen to be minimized is relatively small, and for most of the quantities, it is known that at least some areas of the Sun are in fact *not* in a minimum state. We have considered five basic approaches: (i) comparing the observed field to a reference field or direction, (ii) minimizing the vertical gradient of the magnetic pressure, (iii) minimizing the vertical current density, (iv) minimizing some approximation to the total current density, and (v) minimizing some approximation to the divergence. In many algorithms, combinations of these approaches are used.

Many of the variations in the results here are caused not by fundamental differences in the underlying assumptions, but rather by the different implementations. That is, the algorithms implement different methods for calculating the potential field, different optimization or minimization schemes, or varying degrees of smoothing performed after an initial resolution is assigned to each pixel. Of the automated methods, those which minimize some measure of the vertical current density in conjunction with minimizing an approximation for the fields' divergence show the most promise (e.g. ME1, ME2, UHIM, NPFC2), and make assumptions which are least obviously violated (an assumption about the vertical derivative of the field, linear force-free or potential, is made). For the other methods, it is clear that the assumptions are violated in some areas: the solar magnetic field is neither potential nor linear force-free, so the acute angle methods must fail; the magnetic pressure increases with height above bald patches (and likely in sunspot canopies), so the magnetic pressure gradient and the minimum structure methods must fail; except possibly in localized regions, the distribution of magnetic shear need not be unimodal, let alone Gaussian, so the minimum shear method must fail. Even when there is a quantity that truly is a minimum for the field, the space of possible ambiguity resolutions can contain many local minima, so that a robust optimization scheme is necessary to reach the true global minimum.

All of the automated methods make use of a potential, linear force free, or similar algorithm, at least as a starting condition. In the calculation of these field models, the treatment of the boundary conditions is important and does affect the final outcome. Some methods assume that the observation is close to disk center and approximate  $B_z$  with  $B_{los}$ ; the Green's function algorithms typically make this assumption. FFT algorithms typically have periodic boundary conditions that can be ameliorated by padding the boundary with zeros, though padding with zeroes may not be appropriate if there is strong field at or near the edge of the field-of-view, as in the arcade in Case #1. The presence of nearby unobserved flux impacts the extrapolations and hence most ambiguity resolution schemes; a large field-of-view is important when resolving the ambiguity. For any automated scheme, it is now clear that attention to the boundary conditions is very important, as there is unlikely to be a single ideal treatment for all observational cases.

Although it clearly scored the highest in the tests presented here, AZAM requires manual input and is not appropriate for automated ambiguity resolution, but it is a good tool for understanding the possibilities for ambiguity resolution in select mag-

netograms. For automated processing, the non-linear minimum energy algorithm scored the best, but it is slow. It would be most appropriate for magnetograms where the correct answer is paramount and the processing time secondary. For reasonably fast and reasonably accurate automated ambiguity resolution, the UH iterative method scored best with the revised NPFC2 algorithm a close second.

#### 4.1. WHERE TO GO FROM HERE?

The exercises undertaken in the NCAR workshop highlight the most common challenges to ambiguity resolution algorithms, and highlight as well some directions to consider for future research. The errors produced by flux imbalance, and the influence of magnetic field just outside the field-of-view, can be mitigated by instruments with larger observing area; the best option of course being routine full-disk observations which will be provided by SOLIS and by HMI on the SDO mission. Still, such a solution is not immediately available without some serious thought: for example, all of the algorithms tested here use Cartesian geometry, and full-disk magnetograms will require the use of spherical geometry, except for isolated active regions. Isolated active regions are, however, the exception rather than the rule since interconnections between active regions and even across the equator are common.

A common approach among the algorithms is to make assumptions concerning the vertical structure of the solar magnetic field. Investigations have inferred the depth- or height-dependence of the magnetic field through sophisticated inversion procedures for the spectropolarimetric data, e.g. the MISMA (Sánchez Almeida, 1997; Sánchez Almeida and Lites, 2000), and SIR (Ruiz Cobo, 1998; Westendorp Plaza *et al.*, 2001) approaches. In general, such inversion algorithms require very high precision spectropolarimetry and large computational efforts, and their applicability to the ambiguity resolution problem has not yet been investigated. More tenable in the short-term is the approach of simultaneous multi-height observations, through either multi-line spectropolarimetry covering heights from the deep photosphere to low corona, or the use of broad lines such that inversions can be performed at multiple heights (Metcalf *et al.*, 1995). Again, whether or not these more sophisticated observations can be routinely applied to the ambiguity-resolution problem is still in the research stage. Additionally, very few instruments have the capability of acquiring such data, and even fewer still will be doing so routinely over the next solar cycle.

What will become routine are temporally well-sampled observations from space-based missions. Although the expected data will have shortcomings to be sure, it will be possible to impose smoothness requirements in the temporal domain in addition to the spatial domain. In this way (albeit with post-facto knowledge of an active region's evolution), the characteristics of different quickly-evolving structures such as emerging flux regions and moving magnetic features, can be treated appropriately. The information gained on a feature's temporal evolution

Table I. Summary of Algorithms.

Method	Quantity minimized	Minimization scheme
Acute Angle	$ \theta_o - \theta_e $	local
Large Scale Potential	$ \theta_o - \theta_e $	scale variation
USM	$ \theta_o - \theta_e - \Delta\theta_{mp} $	local
Magnetic Pressure Gradient	$\partial B^2 / \partial z$	local
Minimum Structure	$\omega_s \partial B / \partial z + \omega_p  J_z $	local+smoothing
NPFC	$ J_z $	iterative
Pseudo-Current	$\int d^2 a J_z^2$	conjugate gradient
UH Iterative	$\int d^2 a J_z^2$	iterative
Minimum Energy	$\int d^2 a ( J  +  \nabla \cdot B )^2$	simulated annealing
AZAM	angle between neighboring pixels	interactive

may help untangle questions of magnetic connectivity and refine at least some of the assumptions required for single “snapshot” magnetograms.

Finally, the workshop highlighted the interesting point that, in fact, only a few quantities are presently considered in resolving the ambiguity. We speculate that perhaps further progress can be made by considering other physical properties of the solar atmosphere.

In the more immediate future, this group plans to apply the more successful algorithms to data with added noise and/or to real solar data, address effects of resolution, and include speed benchmark comparisons. The simulated data used here to test the different methods are noise-free. A proper treatment of the noise is beyond the scope of this paper, but we do plan to address the effects of noise on ambiguity resolution in a separate article. By applying the lessons learned during the workshop to improve the ambiguity resolution algorithms, we will ultimately be in a better position to test the algorithms on more difficult and realistic problems.

### Acknowledgements

We thank Y. Fan for providing one of the datasets used to compare the ambiguity resolution algorithms, and Louise Beierle for her efforts in making the workshop a success. The National Center for Atmospheric Research is sponsored by the National Science Foundation. The National Solar Observatory is operated by the Association of Universities for Research in Astronomy, Inc (AURA) for the National Science Foundation. Logistical support for this research was provided by the Helioseismic and Magnetic Imager (HMI) project through NASA Grant NAS5-02139. Logistical support was also provided by the NCAR Strategic Initiative

Table II. Results for Ambiguity Resolution Algorithms.

Solution	Fluxtube and arcade				Multi-pole at $\mu \neq 1.0$			
	$\mathcal{M}_{\text{area}}$	$\mathcal{M}_{\text{flux}}$	$\mathcal{M}_{B_h(s)}$	$\mathcal{M}_{J_z}$	$\mathcal{M}_{\text{area}}$	$\mathcal{M}_{\text{flux}}$	$\mathcal{M}_{B_h(s)}$	$\mathcal{M}_{J_z}$
<b>Acute Angle (potential, FFT)</b>								
NJP (J. Jing)	0.67	0.49	0.92	-0.07	0.76	0.85	0.87	0.10
YLP (Y. Liu)	0.64	0.54	0.90	-0.08	0.82	0.86	0.88	0.08
KLP (K.D Leka)	0.75	0.69	0.94	0.25	0.64	0.90	0.73	0.20
<b>Acute Angle (potential, Greens Func.)</b>								
BBP (V. Yurchyshyn)	0.72	0.65	0.92	0.04	0.78	0.88	0.90	0.25
JLP (J. Li)	0.70	0.64	0.90	-0.01	0.71	0.81	0.83	0.13
<b>Acute Angle (LFFF)</b>								
HSO (H.N. Wang)	0.87	0.70	0.99	0.68	0.85	0.94	0.94	0.60
<b>Large Scale Potential</b>								
LSPM (A. Pevtsov)	0.69	0.53	0.89	-0.84	0.69	0.89	0.74	-0.38
<b>Uniform Shear Method</b>								
USM (Y.-J. Moon)	0.83	0.66	1.00	0.50	0.82	0.90	0.89	0.41
<b>Magnetic Pressure Gradient</b>								
MPG (J. Li)	0.74	0.92	0.85	-0.77	0.67	0.79	0.76	-0.41
<b>Minimum Structure</b>								
MS (M. Georgoulis)	0.22	0.14	0.23	0.18	0.36	0.67	0.58	-0.29
<b>Nonpotential Magnetic Field Calculation</b>								
NPFC (M. Georgoulis, original)	0.70	0.62	0.92	0.02	0.70	0.90	0.83	-0.00
NPFC2 (M. Georgoulis, revised)	0.90	0.77	1.00	0.81	0.99	1.00	1.00	0.98
<b>Pseudo-Current</b>								
PCM (A. Gary)	0.78	0.49	0.98	0.54	0.77	0.82	0.82	0.40
<b>UH Iterative</b>								
UHIM (K. Leka)	0.97	0.91	1.00	0.88	0.97	0.99	1.00	0.97
<b>Minimum Energy</b>								
ME1 (T. Metcalf, original)	0.98	0.96	1.00	0.93	1.00	1.00	1.00	0.99
ME2 (T. Metcalf, non-linear)	1.00	0.99	1.00	0.97	1.00	1.00	1.00	1.00
<b>AZAM</b>								
AZAM (B. Lites)	1.00	1.00	1.00	1.00	1.00	1.00	1.00	1.00
<b>Acute Angle (conducting walls, FFT)</b>								
TMC (T. Metcalf)	0.83	0.94	0.91	0.39	–	–	–	–

Community Spectro-polarimetric Analysis Center (CSAC). TRM, KDL, and GB acknowledge funding from NASA/LWS under contract NNH05CC49C.

## References

- Abramenko, V. I.: 1986, *Solnechnye Dann. Bull. Akad. Nauk SSSR* **8**, 83.
- Alissandrakis, C. E.: 1981, *Astron. Astrophys.* **100**, 197.
- Aly, J. J.: 1988, *Astron. Astrophys.* **203**, 183.
- Canfield, R. C., de La Beaujardière, J. F., Fan, Y., Leka, K. D., McClymont, A. N., Metcalf, T., Mickey, D. L., Wülser, J.-P., and Lites, B. W.: 1993, *Astrophys. J.* **411**, 362.
- Chiu, Y. T. and Hilton, H. H.: 1977, *Astrophys. J.* **212**, 873.
- Cuperman, S., Li, J., and Semel, M.: 1992, *Astron. Astrophys.* **265**, 296.
- Cuperman, S., Li, J., and Semel, M.: 1993, *Astron. Astrophys.* **268**, 749.
- Cuperman, S., Ofman, L., and Semel, M.: 1990, *Astron. Astrophys.* **227**, 583.
- Elmore, D. F., Lites, B. W., Tomczyk, S., Skumanich, A. P., Dunn, R. B., Schuenke, J. A., Stenander, K. V., Leach, T. W., Chambellan, C. W., and Hull, H. K.: 1992, in D. H. Goldstein and R. A. Chipman (eds.), *Polarization Analysis and Measurement, Proc. SPIE* **1746**, 22.
- Fan, Y. and Gibson, S. E.: 2003, *Astrophys. J.* **589**, L105.
- Fan, Y. and Gibson, S. E.: 2004, *Astrophys. J.* **609**, 1123.
- Gary, G. A.: 1989, *Astrophys. J. Suppl.* **69**, 323.
- Gary, G. A. and Démoulin, P.: 1995, *Astrophys. J.* **445**, 982.
- Georgoulis, M. K.: 2005, *Astrophys. J.* **629**, L69.
- Georgoulis, M. K., LaBonte, B. J., and Metcalf, T. R.: 2004, *Astrophys. J.* **602**, 446.
- Gibson, S. E., Fan, Y., Mandrini, C., Fisher, G., and Démoulin, P.: 2004, *Astrophys. J.* **617**, 600.
- Harvey, J. W.: 1969, Ph.D. Thesis, University of Colorado.
- Ichimoto, K. and Solar-B Team: 2005, *J. Korean Astron. Soc.* **38**, 307.
- Jones, H. P., Harvey, J. W., Henney, C. J., Hill, F., and Keller, C. U.: 2002, in H. Sawaya-Lacoste (ed.), *Magnetic Coupling of the Solar Atmosphere, ESA SP-505*, p.15.
- Keil, S. L., Rimmele, T., Keller, C. U., Hill, F., Radick, R. R., Oschmann, J. M., Warner, M., Dalrymple, N. E., Briggs, J., Hegwer, S. L., and Ren, D.: 2003, in S. L. Keil and S. V. Avakyan (eds.), *Innovative Telescopes and Instrumentation for Solar Astrophysics, Proc. SPIE* **4853**, 240.
- Kirkpatrick, S., Gelatt, C. D., and Vecchi, M. P.: 1983, *Science* **220**, 671.
- Leka, K. D.: 1999, *Solar Phys.* **188**, 21.
- Leka, K. D., Fan, Y., and Barnes, G.: 2005, *Astrophys. J.* **626**, 1091.
- Leka, K. D. and Metcalf, T. R.: 2003, *Solar Phys.* **212**, 361.
- Leka, K. D. and Skumanich, A.: 1999, *Solar Phys.* **188**, 3.
- Metcalf, T. R.: 1994, *Solar Phys.* **155**, 235.
- Metcalf, T. R., Jiao, L., McClymont, A. N., Canfield, R. C., and Uitenbroek, H.: 1995, *Astrophys. J.* **439**, 474.
- Metropolis, N., Rosenbluth, A., Rosenbluth, M., Teller, A., and Teller, E.: 1953, *J. Chem. Phys.* **21**, 1087.
- Moon, Y.-J., Wang, H., Spirock, T. J., Goode, P. R., and Park, Y. D.: 2003, *Solar Phys.* **217**, 79.
- Pevtsov, A. A., Canfield, R. C., and Metcalf, T. R.: 1994, *Astrophys. J.* **425**, L117.
- Pevtsov, A. A., Canfield, R. C., and Metcalf, T. R.: 1995, *Astrophys. J.* **440**, L109.
- Ruiz Cobo, B.: 1998, *Astrophys. Space Sci.* **263**, 331.
- Sánchez Almeida, J.: 1997, *Astrophys. J.* **491**, 993.
- Sánchez Almeida, J. and Lites, B. W.: 2000, *Astrophys. J.* **532**, 1215.

- Scherrer, P. H., Bogart, R. S., Bush, R. I., Hoeksema, J. T., Kosovichev, A. G., Schou, J., Rosenberg, W., Springer, L., Tarbell, T. D., Title, A., Wolfson, C. J., Zayer, I., and MDI Engineering Team: 1995, *Solar Phys.* **162**, 129.
- Scherrer, P. H. and HMI Team: 2005, *AGU Spring Meeting Abstr.* #SP43A-05.
- Semel, M. and Skumanich, A.: 1998, *Astron. Astrophys.* **331**, 383.
- Shimizu, T.: 2004, in T. Sakurai and T. Sekii (eds.), *The Solar-B Mission and the Forefront of Solar Physics*, *Astron. Soc. Pacific Conf. Ser.* **325**, 3.
- Titov, V. S., Priest, E. R., and Démoulin, P.: 1993, *Astron. Astrophys.* **276**, 564.
- Wang, H.: 1997, *Solar Phys.* **174**, 265.
- Wang, H., Yan, Y., and Sakurai, T.: 2001, *Solar Phys.* **201**, 323.
- Westendorp Plaza, C., del Toro Iniesta, J. C., Ruiz Cobo, B., Pillet, V. M., Lites, B. W., and Skumanich, A.: 2001, *Astrophys. J.* **547**, 1130.
- Zhang, H.: 2001, *Astrophys. J.* **557**, L71.